Fracture Analysis of a Cycloidal Gearbox as a Yaw Drive on a Wind Turbine

Jairo Aparecido Martins
DESCH North America, Cambridge, Ontario, Canada
jairo.martins@desch.com

Estaner Claro Romao
University of Sao Paulo, Brazil
estaner23@usp.br (corresponding author)

Received: 11 November 2023 | Revised: 25 November 2023 | Accepted: 1 December 2023

 DOI: https://doi.org/10.48084/etasr.6613

ABSTRACT

Fast growth of renewable energies has required addressing challenges such as generating the largest energy production possible throughout the equipment's lifespan and between its preventive and corrective maintenance intervals. Actions such as preventive maintenance, and improvement of the main components, mainly when it comes to reliability and predictability are of extreme importance to reach maximum generation. Due to the importance of the yaw drives for wind turbines, this paper aims to evaluate a failure that occurred on a cycloidal gearbox used in a drive of this kind. For the evaluation of the yaw drive, all the components were analyzed to determine the incurred fracture mechanism. Such analysis was performed by mapping all components, conducting a hardness test to check the components' mechanical properties, analysis of the fractured surfaces of the cycloidal disc, and numerical simulation (linear elastic) via the Finite Element Method (FEM) to check the stress distribution on the fractured part (cycloidal disc) under load, and theoretical calculation of the cycloidal disc lifespan. In addition, the stress distribution by FEM was compared with the broken regions of the physical part. To sum up, after all the evaluations, it is possible to claim the results demonstrate there was a premature fracture of the cycloidal disc that occurred due to the phenomenon of high cycle fatigue.

Keywords-fracture analysis; yaw drive; numerical simulation; Finite Element Method (FEM)

I. INTRODUCTION

Renewable energy is the spinal column of any energy source shifting to fulfill a net zero emission [1]. Consequently, there are many machines and pieces of equipment that aim to utilize renewable sources like harvesting air flow or transforming sun energy into electricity, and for this purpose, continuous efforts have been made to combine both technologies [2, 3]. Particularly about windmill projects [4-6], which is the topic covered in this paper, the highest energy efficiency is obtained when the windmill harvests the maximum amount of energy from different currents of airflow throughout the maximum number of days possible. To reach the objective of maximum power from a machine, it must perform at its maximum resource and its components must have a predictable life. For that, preventive maintenance and operation variable monitoring are instrumental [7, 8]. This challenge ends up motivating scientists and engineers to strive to raise the performance and promote the improvement of these components. In this context, important patents have been registered worldwide [4, 9] along with many published scientific papers that have helped to improve the machine components' performance [10, 11]. Particularly about yaw drives, there are multiple brands and models in the market, the most common designs have multiple stage planetary stages that generate low speed and torque according to the needs [12]. However, there is another type, called cycloidal planetary transmissions, which delivers the advantage over the classic transmissions due to its inverter or involute planetary gears. These drives are smaller, silent, work smoothly, are efficient, and deliver a high gear value, which could be translated as higher power density [13-15].

The novelty of this paper resides in presenting a fracture of cycloidal yaw drives, which is not found in the literature. This paper aims to provide an analysis of the components of the yaw gearbox like bearings, crankshafts, pinion, housings, gears, cycloidal disc, etc., providing a diagnosis of the gearboxes and determining the root cause for equipment failure. The yaw drive evaluated was a cycloidal gearbox with a spur gear stage and a second cycloidal stage [16, 17] driven by four crankshafts.

II. MATERIALS AND METHODS

For disassembling the yaw gearbox, regular wrenches and a hydraulic press were utilized to remove the output gear from the pinion shaft. In addition, mapping and visual inspection of all the parts were conducted along with identification per

disassembly phase/stage. The fractured surfaces passed through visual analysis by comparing the fractured surfaces with the literature [24-25]. Moreover, hardness test of the parts was performed by using a portable hardness tester, Accusize Tool Hardness Tester NIST traceable, and a 3D model was produced in Autodesk F-360 [18] along with a Finite Element Method (FEM) final analysis [19-30]. With those data, it was possible to predict the lifespan of the cycloidal disc as [21-24].

$$\sigma_a = \frac{\Delta\varepsilon_e}{2}.E = \sigma'_f.(2N)^b$$

$$\therefore \frac{\Delta\varepsilon_e}{2}.E = 2N = \left(\frac{\sigma_a}{\sigma'_f}\right)^{\frac{1}{b}} \quad (1)$$

where σ_a is the alternating stress amplitude, $\Delta\varepsilon_e/2$ the elastic strain amplitude under load (mm), E is Young's Module (210,000 MPa), σ'_f is the fatigue strength coefficient, $2N$ is the number of reversals to failure, and b is the fatigue strength exponent.

III. RESULTS AND DISCUSSION

The gearbox was received on a pallet with transversal wood bars to protect it against impacts (Figure 1). A total of 4 gearboxes were delivered, but only one of them passed through analysis. The electrical motor was not included in the pallet. From the outside, there is no damage in the housing, oil leakage, plugs missing, or screws. Furthermore, the output pinion does not contain corrosion or damage to the gear teeth.

Fig. 1. Yaw gearboxes as received.

Figure 2 illustrates the disassembled output gear, the main shaft, and its spline. It can be seen that although the output gear is not damaged, it has corrosion on the internal spline. The body of the main shaft shows profound dents and small scratches certainly produced during the internal collision of pieces of metal. As a common knowledge in the cycloidal gearbox, the cycloidal discs are those that transfer the highest torque, therefore, the ones more likely to have high stresses. Another checking point was the condition of the spur gears in the first stage (Figure 3). They are in good condition, with no marks, high wearing, or deep corrosion identified.

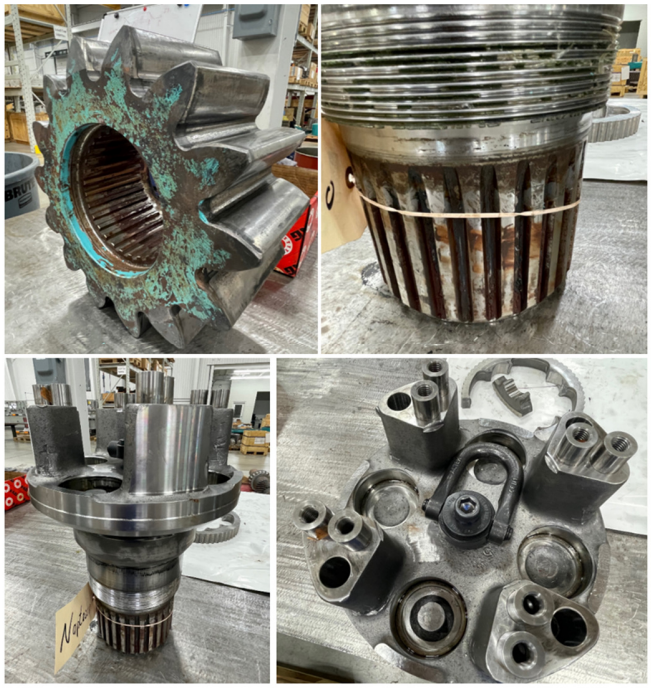

Fig. 2. Output gear, shaft spline with its upper base.

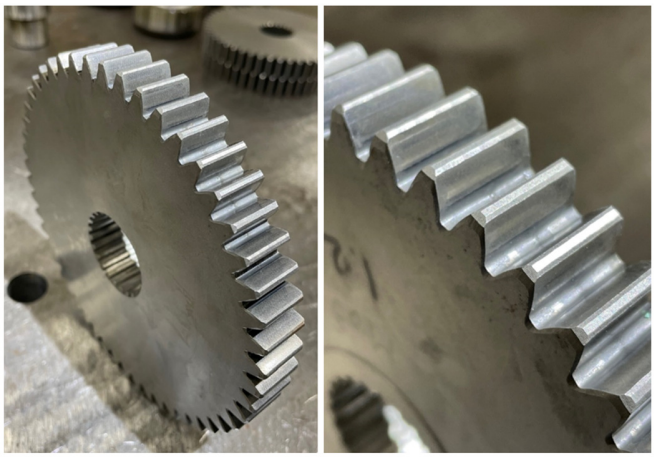

Fig. 3. Stage 1 Spur gears and teeth condition.

The disassembling process continued, and the second stage was reached, where a major collapse occurred. To better map the failure, the cycloidal disc legs were labeled with letters from A to H to have a better understanding of the fracture mechanism of each fractured location, and further on to analyze them as pieces of the whole part (Figure 4).

Figure 5 shows that legs A and B had, as indicated by arrows, two crack nucleation spots at leg A were verified as well as a crack starting on the casting at Leg B at the right downside of the figure. As a highlight, between legs, A and B, the bearing bores are located. Figure 6 on the left (Leg C) shows a final fracture on the cross-section, which differs from the right side (Leg D) where a crack initiated on the opposite side of the bearing bore (corner) but moved towards it and another at the bearing bore surface.

Fig. 4. Overview of the cycloidal disc.

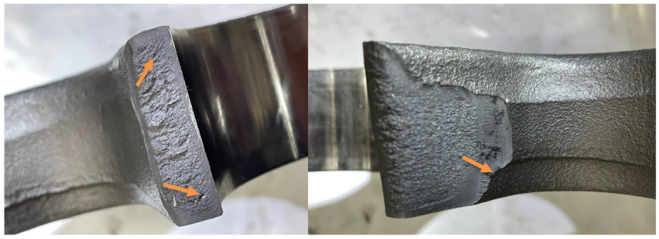

Fig. 5. Leg A (left) and Leg B (right) – arrows indicate crack nucleation.

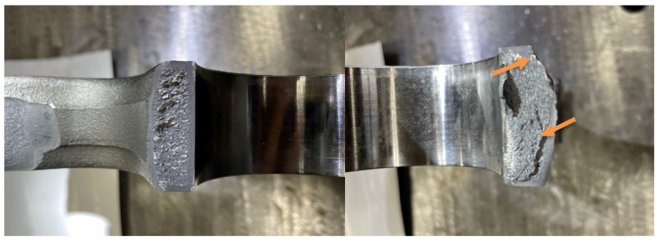

Fig. 6. Leg C (left) and D (right) – arrows indicate crack nucleation spots.

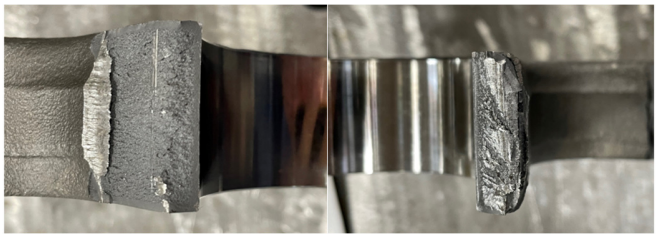

Fig. 7. Leg E (left) and F (right).

On the left side of Figure 7 (Leg E) a double layer of material is verified which suggests an underlayer, where a crack began, and an abrupt detachment happened before the final failure. On the right, (Leg F) an intense fretting after the final fracture is suggested [29]. The arrow in the left of Figure 8 (Leg G) reveals a crack initiating at the corner of the cross-section at the casting side of the part, Figure 8 (right – Leg H) shows at least two points of crack nucleation with a perceptible distance between the beach marks, probably because of due to a more intense strain cycling close to the part collapse [25].

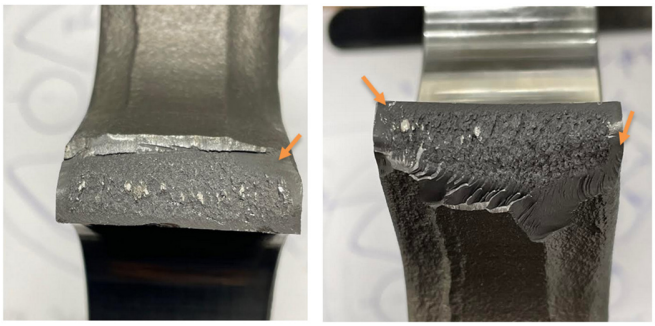

Fig. 8. Leg G (left) and H (right)- arrows indicate cracks in nucleation spots.

Fig. 9. Broken part of the cycloidal disc showing multiple cracks – arrows on both sides indicate the regions verified in Figure 11, the center arrow pointing to G shows multiple cracks.

The central arrow in Figure 9 reveals multiple cracks on the Leg G surface and large deformations, which indicate a high level of stress in multiple directions, suggesting torsional loading as well as radial and axial ones, most likely due to the high instability throughout the fracture process. Figure 10 shows the outer fracture of the cycloidal disc close to Legs G and H, as indicated in Figure 9 by arrows on both sides. Leg G on the left side, shows the crack initiating on the external side of the bearing bore (casting), while in Leg H the crack started at the external diameter of the cycloidal disc.

The crankshafts were analyzed in terms of major deformations. All shafts show deep plastic deformation on the bearing region. Those deformations are due to high pressure by the bearing rolls on the shaft surface during failure (Figure 11). The bearings were also evaluated and visually checked for dents, marks, or corrosion. Although they are in good condition, the regular procedure for every service is to replace them due to clearance uncertainty (Figure 12).

Fig. 10. Leg G (left) and Leg H (right) – arrows show the crack nucleation spots.

Fig. 11. Crankshaft.

Fig. 12. Bearing that drives the cycloidal disc.

The output flange in Figure 13 shows a solid part with no deformations, only a few expected scratches during operation and disassembling.

Fig. 13. Output flange.

Another characteristic evaluated during the failure analysis was the part's hardness, which aimed to check any inconsistency with regular gearbox designs. Table I illustrates the values measured on each part. The harnesses are according to the expected values utilized in designing gearboxes, except the output flange's lower value, even though these parts did not contribute to the failure. After the hardness measurement, 3D modeling was produced, and just after that Finite Element Method (FEM) calculation was executed (Figure 14) to verify whether the highest stress spots were the ones where the cracks initiated. The 3D modeling took into consideration the dimensions of the physical part (cycloidal disc). The mesh applied was a tetrahedral element (parabolic functions), with maximum turn angle on curves of 10 degrees, maximum adjacent mesh size ratio of 1.5, maximum aspect ratio of 10, and minimum element size of 20% of the average size. The center bore had a frictionless constraint on it, the pins on the external side of the cycloidal disc were fixed for all directions (u_x, u_y, and u_z) and the load was applied on every bearing bore where the crankshaft drives the cycloidal discs, exactly as the gearbox works. For the numerical FEM simulation, a nominal torque of 12,250 Nm was applied, which was based on the model of the gearbox [18].

TABLE I. HARDNESS OF EACH COMPONENT

Part	Description	Measured
1	Spur gear	55 HRC
2	Output flange	220 HB
3	Crankshaft	59 HRC
4	Cycloidal disc – close to the external diameter	60 HRC
5	Cycloidal disc – close to the centered bore	55 HRC

Fig. 14. 3D modeling and mesh applied on the cycloidal disc.

Figure 15 presents the regions with the higher stresses located at the external radius in the groove close to the disc external diameter (170.2 MPa) and regions on the same profile but now on the flat surface that neighbors the bearing bore (75.1 MPa). Those regions on the cycloidal disc coincide with the cracks-initiated regions at the part. However, the stress level is expressively low when compared to the hardened material's mechanical strength [25].

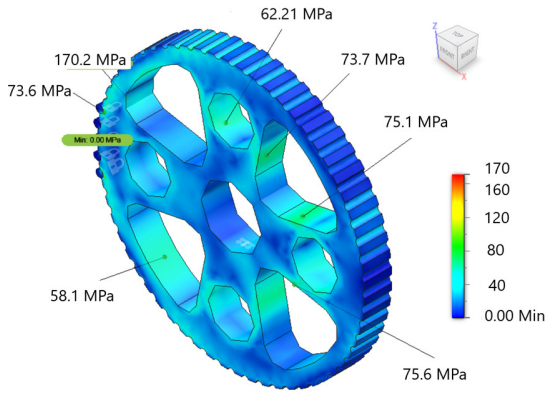

Fig. 15. Output results from the FEM calculations.

Based on the FEM calculations and the number of cycles to fracture under normal conditions for this application, the fatigue is considered high-cycle fatigue, which means it is characterized as having a low-strain regime where the nominal strain is linear elastic. Therefore, as mentioned above, the number of cycles to fatigue was determined by (1). Since the chemical composition or the metallurgical condition of the parts were not determined, and only their hardness was measured, there was a need to assume materials with similar hardnesses, particularly for the disc. The values assumed for the calculation were from two similar materials, SAE 1045 quenched and tempered (Q&T) to 180ºC, and the material 35CrMo quenched and tempered (Q&T) to 400ºC, both materials usually applied as materials for gearbox parts. Table II shows the expected high cycle fatigue of similar materials used as references.

TABLE II. MATERIALS USED TO CALCULATE THE HIGH-CYCLE LIFETIME

Material	Q&T	σ'_f	b	2N
SAE 1045 [25]	180 ºC	2,261	-0.089	4.24×10^{12}
35CrMo [29]	400 ºC	2,030	-0.081	1.98×10^{13}

The obtained values couldn't be reached during the whole yaw drive lifespan, which suggests abnormalities on the cycloidal disc during operation. As a reference, the material 35CrMo might have a stress amplitude of 550 MPa for an infinite fatigue life ($>10^6$ cycles) – based on the S-N curve – which is much higher than the 170.2 MPa calculated via FEM.

IV. CONCLUSIONS

Although there was a high level of damage in the cycloidal gearbox, particularly on the cycloidal disc, the failure did not occur due to high impacts or intense vibrations during operation. A progressive failure occurred, evidenced by the nucleation of multiple cracks, their propagation, and ending up to the final failure of the cycloidal disc. Furthermore, despite the Finite Element Method showing some spots as candidates to nucleate cracks under cyclical loading, the additional regions where multiple cracks started even under low-stress levels suggest that the parts experienced many loads as torque and forces on orthogonal axes. The failure is considered abnormal and unexpected because the theoretical number of cycles, under normal conditions of operation, is expressively larger than any yaw drive operation, which means the cycloidal disc is the last part to fail, after roller bearings, crankshafts, etc.

To sum up, it is possible to conclude that premature failure occurred due to the phenomena of high-cycle fatigue, which disregard the possibilities of either high impacts or vibrations during operation. The abnormalities' most likely root causes might be related to problems with the casting, heat treatment, or retained austenite in the microstructure, temper, or hydrogen embrittlement. To reach a profound evaluation and solid conclusion, the use of an SEM microscope is necessary, which will be covered in a following paper.

ACKNOWLEDGMENT

The authors would like to thank Frank Laudahn (R&D technician), Markus Pape (Engineering Manager), and Stephen Pack (C.O.O) from DESCH North America for their support and collaboration during this research project.

REFERENCES

[1] IEA, *Renewables 2021 - Analysis and forecast to 2026*. Paris, France: International Energy Agency, 2021.

[2] M. Mahmoud, M. Ramadan, A.-G. Olabi, K. Pullen, and S. Naher, "A review of mechanical energy storage systems combined with wind and solar applications," *Energy Conversion and Management*, vol. 210, Apr. 2020, Art. no. 112670, https://doi.org/10.1016/j.enconman.2020.112670.

[3] J. A. Ferraz de Andrade Santos, P. de Jong, C. Alves da Costa, and E. A. Torres, "Combining wind and solar energy sources: Potential for hybrid power generation in Brazil," *Utilities Policy*, vol. 67, Dec. 2020, Art. no. 101084, https://doi.org/10.1016/j.jup.2020.101084.

[4] S. Usha, M. S. Abishake, G. Anbezhil, and S. Dhanasekar, "Increasing the wind power generation by modifying the windmill mechanism," *Materials Today: Proceedings*, vol. 72, pp. 3075–3080, Jan. 2023, https://doi.org/10.1016/j.matpr.2022.09.250.

[5] W. J. Florkowski and J. Rakowska, "Review of Regional Renewable Energy Investment Projects: The Example of EU Cohesion Funds Dispersal," *Sustainability*, vol. 14, no. 24, Jan. 2022, Art. no. 17007, https://doi.org/10.3390/su142417007.

[6] M. F. Hairani and S. A. Jumaat, "Development of Double Mini Windmill with Smart Monitoring System," *Journal of Electronic Voltage and Application*, vol. 3, no. 2, pp. 59–66, Dec. 2022.

[7] R. Zheng, Y. Zhou, and Y. Zhang, "Optimal preventive maintenance for wind turbines considering the effects of wind speed," *Wind Energy*, vol. 23, no. 11, pp. 1987–2003, 2020, https://doi.org/10.1002/we.2541.

[8] Y. Aafif, A. Chelbi, L. Mifdal, S. Dellagi, and I. Majdouline, "Optimal preventive maintenance strategies for a wind turbine gearbox," *Energy Reports*, vol. 8, pp. 803–814, Nov. 2022, https://doi.org/10.1016/j.egyr.2022.07.084.

[9] T. L. Baun, "Wind Turbine Generator with Service Platform and Associated Method," US20230059355A1.

[10] *Guidelines for Design of Wind Turbines*, 2nd ed. Copenhagen, Denmark: DNV/Risø, 2002.

[11] M.-G. Kim and P. H. Dalhoff, "Yaw Systems for wind turbines – Overview of concepts, current challenges and design methods," *Journal of Physics: Conference Series*, vol. 524, no. 1, Mar. 2014, Art. no. 012086, https://doi.org/10.1088/1742-6596/524/1/012086.

[12] "Wind Turbine Yaw System: Introduction," *Windmills Tech*, Nov. 17, 2022. https://windmillstech.com/wind-turbine-yaw-system-introduction/.

[13] S. Bednarczyk, "Cycloidal Planetary Transmission," Ph.D. dissertation, Wroclaw University of Technology, Wroclaw, Poland, 2014.

[14] M. Wiklo, R. Krol, K. Olejarczyk, and K. Kolodziejczyk, "Output torque ripple for a cycloidal gear train," *Proceedings of the Institution of Mechanical Engineers, Part C: Journal of Mechanical Engineering Science*, vol. 233, no. 21–22, pp. 7270–7281, Nov. 2019, https://doi.org/10.1177/0954406219841656.

[15] K. Olejarczyk, M. Wiklo, and K. Kolodziejczyk, "The cycloidal gearbox efficiency for different types of bearings—Sleeves vs. needle bearings," *Proceedings of the Institution of Mechanical Engineers, Part C: Journal of Mechanical Engineering Science*, vol. 233, no. 21–22, pp. 7401–7411, Nov. 2019, https://doi.org/10.1177/0954406219859903.

[16] "Design and Engineering," Innovative Automation, Aug. 31, 2022. https://www.innovativeautomation.com/capabilities/design-engineering/.

[17] "RV-500N." https://quickfinder.nabtesco.de/en/component/k2/166-rv-500n.

[18] "Fusion 360 Help ," Autodesk, https://help.autodesk.com/view/fusion360/ENU/?guid=GUID-1C665B4D-7BF7-4FDF-98B0-AA7EE12B5AC2.

[19] J. A. Martins and E. C. Romao, "The Importance of Accurate Boundary Condition in Obtaining Reliable Shearing Stresses on a Torsional Finite Element Simulation," *Engineering, Technology & Applied Science Research*, vol. 12, no. 3, pp. 8482–8487, Jun. 2022, https://doi.org/10.48084/etasr.4708.

[20] E. C. Romao and L. F. M. de Moura, "3D contaminant transport by GFEM with hexahedral elements," *International Communications in Heat and Mass Transfer*, vol. 42, pp. 43–50, Mar. 2013, https://doi.org/10.1016/j.icheatmasstransfer.2012.10.016.

[21] J. A. Martins and E. C. Romao, "Analyzing 2D segment by Multiphysics in heat transfer and solid mechanics, pondering variables by Design of Experiment (DOE)," *Engineering Science and Technology, an International Journal*, vol. 19, no. 4, pp. 1929–1935, Dec. 2016, https://doi.org/10.1016/j.jestch.2016.10.013.

[22] E. C. Romao and L. H. P. de Assis, "Numerical Simulation of 1D Unsteady Heat Conduction-Convection in Spherical and Cylindrical Coordinates by Fourth-Order FDM," *Engineering, Technology & Applied Science Research*, vol. 8, no. 1, pp. 2389–2392, Feb. 2018, https://doi.org/10.48084/etasr.1724.

[23] W. R. do P. Junior, J. A. Martins, and E. C. Romao, "Utilizing Numerical Simulations to Analyze the Efficiency of a Porous Reactor," *Engineering, Technology & Applied Science Research*, vol. 12, no. 3, pp. 8755–8759, Jun. 2022, https://doi.org/10.48084/etasr.4957.

[24] G. E. Dieter, *Mechanical Metallurgy*. New York, NY, USA: Mc Graw-Hill, 1986.

[25] R. W. Hertzberg, R. P. Vinci, and J. L. Hertzberg, *Deformation and Fracture Mechanics of Engineering Materials*, 5th edition. Hoboken, NJ, USA: Wiley, 2012.

[26] F. Kun, H. A. Carmona, J. S. Andrade, and H. J. Herrmann, "Universality behind Basquin's Law of Fatigue," *Physical Review Letters*, vol. 100, no. 9, Mar. 2008, Art. no. 094301, https://doi.org/10.1103/PhysRevLett.100.094301.

[27] H. Mughrabi and H. W. Hoppel, "Cyclic deformation and fatigue properties of very fine-grained metals and alloys," *International Journal of Fatigue*, vol. 32, no. 9, pp. 1413–1427, Sep. 2010, https://doi.org/10.1016/j.ijfatigue.2009.10.007.

[28] S. Kwofie, "An exponential stress function for predicting fatigue strength and life due to mean stresses," *International Journal of Fatigue*, vol. 23, no. 9, pp. 829–836, Oct. 2001, https://doi.org/10.1016/S0142-1123(01)00044-5.

[29] M. Yang *et al*., "High-Cycle Fatigue Behavior and Fatigue Strength Prediction of Differently Heat-Treated 35CrMo Steels," *Metals*, vol. 12, no. 4, Apr. 2022, Art. no. 688, https://doi.org/10.3390/met12040688.

[30] D. G. Zisopol, D. V. Iacob, and A. I. Portoaca, "A Theoretical-Experimental Study of the Influence of FDM Parameters on PLA Spur Gear Stiffness," *Engineering, Technology & Applied Science Research*, vol. 12, no. 5, pp. 9329–9335, Oct. 2022, https://doi.org/10.48084/etasr.5183.